Int J Appl Earth Obs Geoinformation 66 (2018) 210–225

Contents lists available at ScienceDirect

Int J Appl Earth Obs Geoinformation

journal homepage: www.elsevier.com/locate/jag

Spatio-temporal analysis of prodelta dynamics by means of new satellite generation: the case of Po river by Landsat-8 data

Ciro Manzo[a,e,*], Braga Federica[b], Zaggia Luca[b], Brando Vittorio Ernesto[d], Giardino Claudia[c], Bresciani Mariano[c], Bassani Cristiana[c]

[a] National Research Council of Italy, Institute for Atmospheric Pollution Research (IIA-CNR), Rome, Italy
[b] National Research Council of Italy, Institute of Marine Sciences (ISMAR-CNR), Venice, Italy
[c] National Research Council of Italy, Institute for Electromagnetic Sensing of the Environment (IREA-CNR), Milan, Italy
[d] National Research Council of Italy, Institute of Atmospheric Sciences and Climate (CNR-ISAC), GOS Team, Rome, Italy
[e] Now at Rhea Group, Frascati (RM), Italy

ARTICLE INFO

Keyword:
Turbidity
Sediment dispersion
Prodelta area
SST
Spatial pattern

ABSTRACT

This paper describes a procedure to perform spatio-temporal analysis of river plume dispersion in prodelta areas by multi-temporal Landsat-8-derived products for identifying zones sensitive to water discharge and for providing geostatistical patterns of turbidity linked to different meteo-marine forcings. In particular, we characterized the temporal and spatial variability of turbidity and sea surface temperature (SST) in the Po River prodelta (Northern Adriatic Sea, Italy) during the period 2013–2016. To perform this analysis, a two-pronged processing methodology was implemented and the resulting outputs were analysed through a series of statistical tools. A pixel-based spatial correlation analysis was carried out by comparing temporal curves of turbidity and SST hypercubes with in situ time series of wind speed and water discharge, providing correlation coefficient maps. A geostatistical analysis was performed to determine the spatial dependency of the turbidity datasets per each satellite image, providing maps of correlation and variograms. The results show a linear correlation between water discharge and turbidity variations in the points more affected by the buoyant plumes and along the southern coast of Po River delta. Better inverse correlation was found between turbidity and SST during floods rather than other periods. The correlation maps of wind speed with turbidity show different spatial patterns depending on local or basin-scale wind effects. Variogram maps identify different spatial anisotropy structures of turbidity in response to ambient conditions (i.e. strong Bora or Scirocco winds, floods). Since the implemented processing methodology is based on open source software and free satellite data, it represents a promising tool for the monitoring of maritime ecosystems and to address water quality analyses and the investigations of sediment dynamics in estuarine and coastal waters.

1. Introduction

River plumes play a fundamental role in the dynamics of coastal areas: with waves and currents they contribute to the distribution of organic and inorganic riverborne particulate thereby affecting not only the morphology, but also the ecology of coastal waters.

Catchment soils, mobilized by weathering and transported into the river network, are eventually transferred and deposited in the proximity of estuaries and deltaic systems (Davidson Arnott, 2010). Furthermore, rivers are a major route through which nutrients, sediments and pollutants, such as heavy metals and organic compounds, are transported (Qin et al., 2007; Rao and Schwab, 2007; Zhang et al., 2016).

In water bodies affected by rivers plumes such as lakes (Zhang et al., 2016) or semi-enclosed coastal regions (Kourafalou, 2001; Brando et al., 2015), the flow and associated suspended matter can alter the physical and biogeochemical properties of the basin, modifying thermohaline and dynamical properties (Horner-Devine et al., 2015), and affecting the exchange of nutrients and the migration of phytoplankton, zooplankton and fish (Rao and Schwab, 2007; Wang et al., 2012; Marini et al., 2008; Tesi et al., 2011). Different processes affect the river plume and its sediments load: advection and mixing drive the general structure of the plume while the along-coast transport of the riverine material is controlled by other processes, including stratified-shear mixing, frontal processes, mesoscale circulation, tide and wind forcing, as well as Coriolis effects (Hetland, 2005; Horner-Devine et al., 2015; Geyer et al., 2004; Nof and Pichevin, 2001).

* Corresponding author at: National Research Council of Italy, Institute for Atmospheric Pollution Research (IIA-CNR), Rome, Italy.
E-mail addresses: ciro.manzo@iia.cnr.it, c.manzo@rheagroup.com (C. Manzo).

https://doi.org/10.1016/j.jag.2017.11.012
Received 3 April 2017; Received in revised form 23 November 2017; Accepted 25 November 2017

Understanding river plume dispersion in prodelta areas and its effects on the coastal environment is however quite challenging as suspended matter vehiculated by the rivers to the coast is highly variable over time depending on the hydrology and the distribution of the precipitation over the catchment. High concentrations of suspended matter in river plumes can affect water quality, generally decreasing light penetration with effects on the growth of aquatic vegetation and consequently the ecology (Kirk, 1994; Gippel, 1995; Milliman and Farnsworth, 2013; Cannizzaro et al., 2013; Dogliotti et al., 2015). For these reasons there is a mounting interest in monitoring the turbidity as an indicator of water quality in estuarine and coastal areas, (i.e., Marine Strategy Framework Directive (MSDF) or Maritime Spatial Planning Directive (MSPD)). Cristina et al. (2015) studied how the remote sensing can play a fundamental role in supporting the MSFD, by the use of MEdium Resolution Imaging Spectrometer (MERIS) sensor products.

The mapping of prodelta area by remote sensing has proven to be a successful methodology for water quality monitoring (Dogliotti et al., 2016, 2015; Braga et al., 2017; Brando et al., 2015; Petus et al., 2014; Nechad et al., 2010) and tracing river plumes (Shen et al., 2010; Falcini et al., 2012; Petus et al., 2010). Earth observation methods provide the synoptic perspective required to identify the plume changing features both in time and space overcoming the problems of spatial and temporal relevance of conventional monitoring techniques.

Satellite sensors such as Advanced Very High Resolution Radiometer (AVHRR), Sea-viewing Wide Field-of-view Sensor (SeaWiFS), Moderate Resolution Imaging Spectroradiometer (MODIS) and Medium Resolution Imaging Spectrometer (MERIS) have been widely used to describe the dynamics and physical characteristics of river plumes, their interaction with coastal forcings and seaward dispersion (Brodie et al., 2010; Doxaran et al., 2012; Filipponi et al., 2014; Dogliotti et al., 2016). Despite the low spatial resolution of these sensors (from 250 m to 4 km) they have provided valuable information on the evolution of river plumes at frequent revisit time from 1 to 3 days (Robinson, 2010). The integration of sea surface temperature (SST) with ocean color radiometry also supported the characterization of these transition ecosystems (Falcini et al., 2012; Otero et al., 2009). Other sensors with better spatial resolution such as Landsat, SPOT, permit more detailed investigations, but their low revisit frequency may reduce the number of available scenes (Zheng et al., 2015; Aldabash and Balik, 2016).

The availability of wide free-access data catalogues encouraged their use in the study of spatio-temporal variability of river plumes in estuaries and coastal waters (Zhang et al., 2010; Nechad et al., 2011; Chen et al., 2011; Shen et al., 2013, 2011; Petus et al., 2014; Filipponi et al., 2015; Dogliotti et al., 2016, 2015). These datasets support the monitoring of river plume dispersion, quantifying their relation to main natural forcings as discharge, waves, current and wind (Zhang et al., 2016, 2014; Ruddick and Lacroix, 2006). However, Pahlevan et al. (2012) evaluated the performances of Landsat-7 imagery for coastal analysis but found that low signal to noise ratio (S/N) and radiometric resolution were not sufficient to perform the analysis with good quality.

River mouth plume-dispersion patterns can be now observed with unprecedented resolution because of the most recent generation of satellite imageries such as those provided by Landsat-8 and Sentinel-2 (Irons et al., 2012; Pahlevan et al., 2014; Gernez et al., 2015; Lavrova et al., 2016). Furthermore, Landsat-8 provided continuity to multi-decadal time series of Landsat scenes allowing to perform long term analysis (Lymburner et al., 2016). Recently this data has been used by Brando et al. (2015) to characterize the Po river plume over the prodelta using SST and ocean color during the flooding event of 2014/11/19.

On the same time there are several processing algorithms devoted to carry out apparent and inherent optical properties and water quality parameters (Chlorophyll − Chla, suspended particulate matter − SPM, and colored dissolved organic matter − CDOM) (Odermatt et al., 2012; Lee et al., 2016a,b herein after). Dogliotti et al., 2015 obtained good performance of the algorithm for retrieval of turbidity from remotely sensed data in different regions using field data in estuarine and coastal waters. This algorithm was then implemented in the software ACOLITE for atmospheric correction and processing of Landsat-8 and Sentinel-2 data (Vanhellemont and Ruddick, 2016, 2015, 2014).

Even if the earth observation products cannot fully replace buoy monitoring or field investigations with oceanographic vessels they reveal multi-scale surficial spatial patterns in different time frames otherwise not observable with conventional methods. The combined use of remote sensing and *in situ* data, and more recently theoretical models, are quite promising for quantifying coastal processes (Bonamano et al., 2016; Brando et al., 2015; Lee et al., 2016a; Braga et al., 2017). Indeed, the integration of satellite-derived product with other multidisciplinary data can become a useful tool for a long-term monitoring system capable of building large data sets for studying these environments (Bonamano et al., 2016; Filipponi et al., 2015). The link between earth observation and models has actually been identified as a critical step in achieving effective integrated ecosystem assessment (Malone et al., 2014).

The development of a new generation of satellite data for ocean color and new data policy for free use of NASA and ESA images significantly extended the amount of information available on different spatial and temporal scales for the study of oceanographic processes and marine ecosystem monitoring. In this context, satellite big data processing is becoming a challenging task due to the extensive nature of the analysis, combined with the large amount of data handled (Ma et al., 2015). Therefore, the capacity to develop specific retrieval algorithms and robust processing techniques for time series analysis is crucial. It is thus necessary to define a reliable processing chain to perform temporal analysis for estuarine and coastal zones.

This paper is part of a research focused on the Po River prodelta, a complex environment located in the northern Adriatic Sea (NAS) Italy, by means of Landsat-8-derived products. This coastal system is dominated by riverine inputs and hydrodynamic forcings, and their interactions influence the physical and biogeochemical processes of the whole basin. The turbidity maps on a shorter temporal range has been just presented by Braga et al. (2017) in order to describe the Po river plumes and provide some interpretation to the controlling factors through time and space. Brando et al. (2015) characterized the river plumes in the NAS during significant flood event in November 2014 adopting Operational Land Imager (OLI) sensor, Thermal Infrared Radiometer Sensor (TIRS) data and hydrodynamic modelling obtaining good correlation between turbidity, SST and salinity showing how they change between different rivers in the NAS. Finally, to complete this research we considered other quantitative indices to extend the analysis of controlling factors, in particular this contribution describes a multi-temporal processing chain based on a workflow written in R language which adds new outputs and maps also introducing the thermal analysis and peak detection methods. The paper is organized according the following sections: the first introduces to the study area providing the environmental setting, the second defines the satellite data and the processing chain. Then the results describe the outputs based on two approaches: punctual extraction of time series from temporal hypercubes and spatial pattern analysis. Finally, we discuss these results in light of comparison with literature and previous researches.

2. Study area

The study area is located in the prodelta of the Po River, the major Italian river for discharge and extension of the drainage basin. The Po River is also the largest tributary of the northern Adriatic Sea (NAS) and its delta extends seaward for about 25 km with five major distributaries characterized by different and variable partitioning of water discharge and sediment load. From North to South these branches are called Maistra, Pila, Tolle, Gnocca, and Goro (Fig. 1). More than half of the total flow and sediment load are carried by the Po di Pila whose outlet

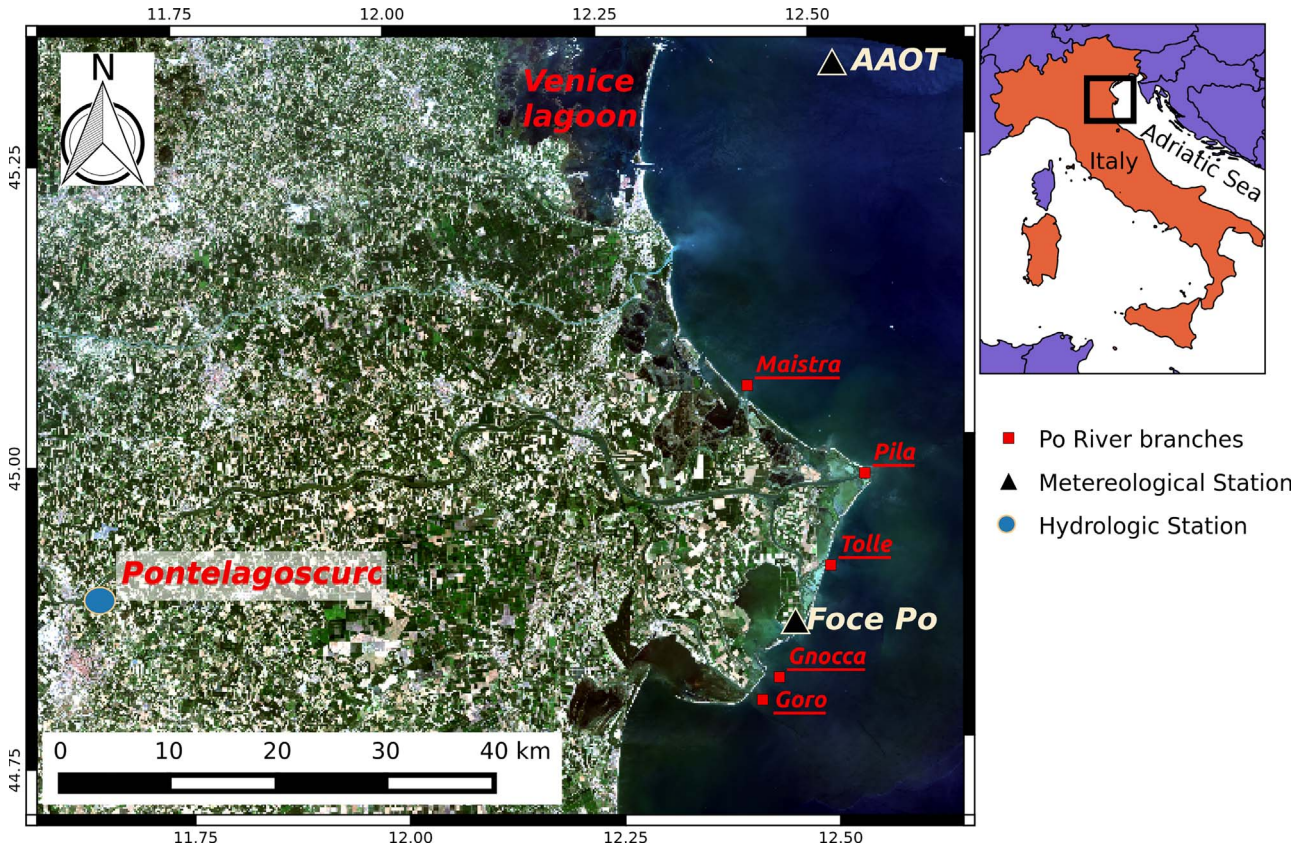

Fig. 1. Po River prodelta with the five distributaries. The triangles are the meteorological stations; the blue circle is the hydrologic station of Pontelagoscuro. (For interpretation of the references to colour in this figure legend, the reader is referred to the web version of this article.)

is located at the apex of the delta (Syvitski et al., 2005; Tesi et al., 2011). This system was subjected to large modifications as an effect of land use and water management in historical time and is presently classified as a river-dominated delta, although delta lobes of each distributary have proper morphologies, accretion rates, prodelta geometry and evolution (Trincardi et al., 2004).

The Po delta system is an important freshwater and sediment input for NAS basin which can be considered a semi-enclosed regional sea (Kourafalou, 2001). Its interaction with the general circulation of the NAS influences the physical and biogeochemical processes of the whole basin (Marini et al., 2008; Solidoro et al., 2009; Tesi et al., 2011).

The river regime is characterized by two dry periods in winter and summer, alternated by two seasonal high-discharge periods in early spring (snow and glacier melting and frontal rainfall) and in late autumn related to the seasonal rainfall (Boldrin et al., 2005; Syvitski and Kettner, 2007).

It is widely recognized that the Po river delta is the main source of sediments for the NAS and its finer suspended fraction ($< 63\,\mu m$) accounts for over 97% of the suspended load (Tesi 2011). Fine sand, silt and clay are mainly supplied from this river and transported southward by the coastal current Western Adriatic Coastal Current (WACC) (Artegiani et al., 1997; Sherwood et al., 2004). Indeed, the main hydrodynamic forcings affecting the Po River prodelta are the NAS cyclonic current and tidal cycle. The combination of wind and thermohaline forcing drive the southward flow of WACC coastal current. Moreover, two distinct wind regimes, the northeasterly Bora and southeasterly Sirocco, can affect basin-wide circulation in the NAS (Orlìc et al., 1994) and control the sediment transport (Friedrichs and Scully, 2007). Therefore, while transport within the buoyant plume is important during floods, wave action and the pattern of currents drive the sediment pathways (Bever et al., 2009). The wave action along the coast in particular in low tide conditions causes a larger sediment resuspension on the seafloor increasing turbidity (Friedrichs and Scully, 2007).

3. Materials and methods

The retrieval of spatial pattern of correlation and variability of the turbidity and SST from Landsat-8 sensors data was performed by a processing chain developed in R language (R Cran Team, 2013) and running in Linux operative system adopting different libraries (Bivand et al., 2013; Hijmans, 2014; Pebesma, 2004) and calling external atmospheric correction program in IDL and Nasa web tool as described in the scheme of Fig. 2.

The optical and thermal satellite data are compared to hydrodynamic forcings, the water discharge and the wind, defining the highest sensitive area, the geometrical patterns of data variability, and the link between turbidity, SST and water discharge during the floods.

3.1. Landsat-8 image processing

The images used in this study are collected by the Operational Land Imager (OLI) sensor and by the Thermal Infrared Radiometer Sensor (TIRS) on board of Landsat-8. OLI sensor has 8 bands the visible, the near and shortwave infrared spectral regions at 30 m in addition to a panchromatic band at 15 m; the TIRS has two bands in the long wave thermal infrared with spatial resolution of 100 m, resampled to 30 m (Irons et al., 2012). Although the revisiting time of Landsat-8 is 16 days, being the study area lays common to path 191 and 192 (raw 29), the scenes were available at intervals of 7 and 9 days.

Landsat-8 images were gathered from Earth Explorer, an USGS web service to search and download data (http://earthexplorer.usgs.gov/). The search tool for the period 2013–2016 in the study area, provided a list of more than 50 images (Fig. 3) images at standard level-one

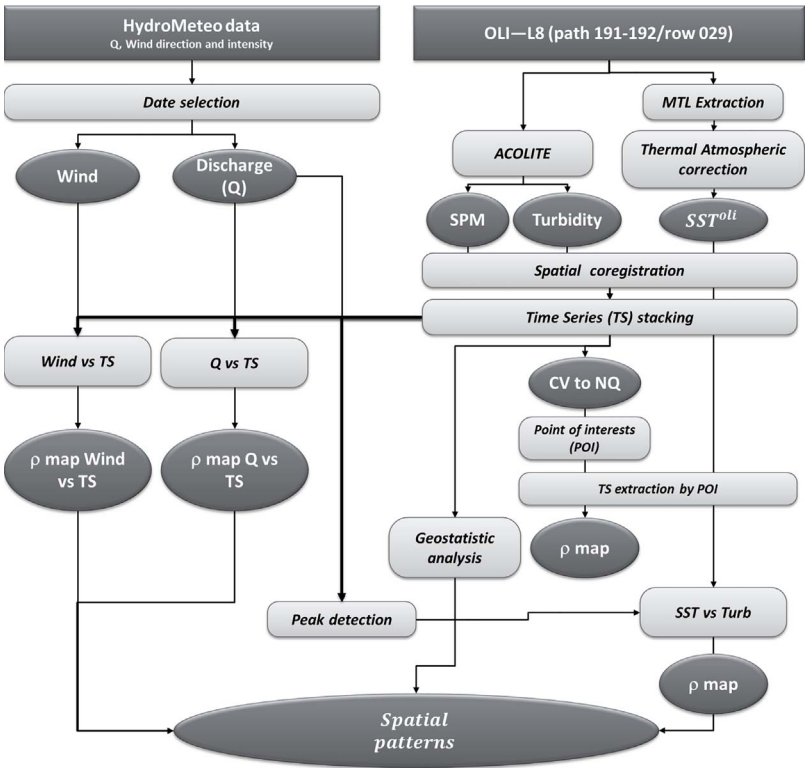

Fig. 2. Processing scheme based on R language, GDAL libraries and IDL.

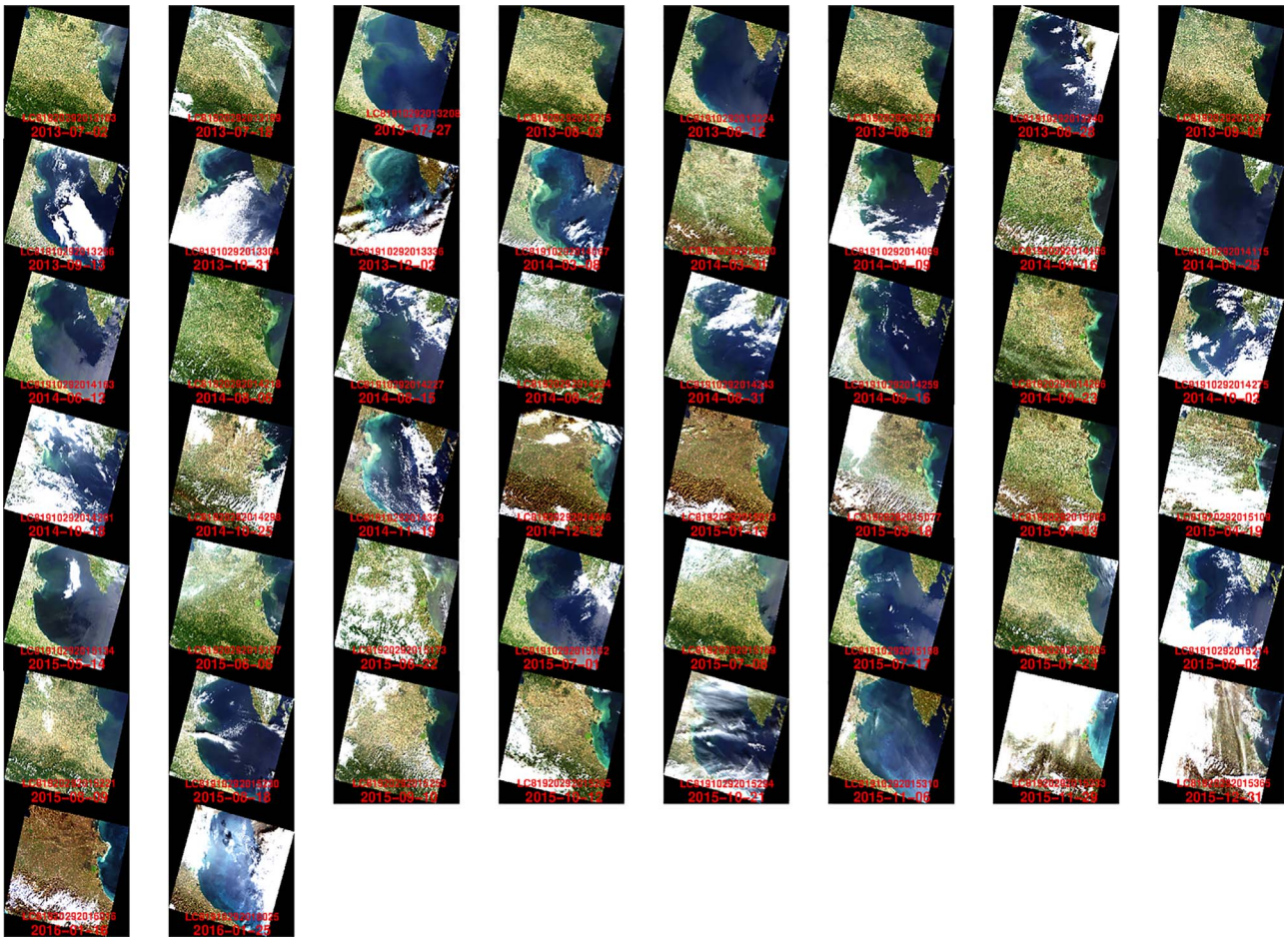

Fig. 3. Pseudo-true-colour composite of Landsat-8 time series 02/07/2013—25/01/2016 (50 observations). Path 191 and 192, Row 029—for daytime overpasses. (For interpretation of the references to colour in this figure legend, the reader is referred to the web version of this article.)

terrain-corrected (L1T) with an averaged Root Mean Square Error (RMSE) < 0.5. We wrote a script able to automatically download the images by excluding those with significant clouds and cirrus, then a selection for excluding sun glint and thick aerosols was performed exporting true color composite and according Franz et al. (2015). The thermal data were available for the entire dataset with exception of the last two Images 16/01/2016–25/01/2016.

OLI images were radiometrically calibrated according to Pahlevan et al. (2014) and then atmospherically corrected with ACOLITE (Atmospheric Correction for OLI 'lite') described in Vanhellemont and Ruddick (2014; 2015). The software was run with a SWIR atmospheric correction mode based on OLI bands 6 and 7 (1609 and 2201 nm) according to Vanhellemont and Ruddick (2015) for moderately to extremely turbid waters. ACOLITE-derived water leaving reflectance ($\rho_w(\lambda)$) was converted in turbidity (T, expressed in formazin nephelometric unit [FNU]) according the (Dogliotti et al., 2015):

$$T = \frac{A_T^{\lambda}\rho w(\lambda)}{(1-\rho w(\lambda)/C^{\lambda}} [\mathrm{FNU}] \quad (1)$$

where A_T and C are two wavelength-dependent calibration coefficients. The parameter C was calibrated using "standard" inherent optical properties (IOPs) as described in Nechad et al. (2010), while the A_T coefficient was obtained by a non-linear least-square regression analysis using in situ measurements of T and $\rho_w(\lambda)$ in various European and South American coastal and estuarine environments.

This algorithm was validated for NAS by Braga et al. (2017) with 32 measurements points, the correlation was statistically significant (r 0.99) and the standard error was 6.2 FNU in the 1–200 FNU turbidity range. The algorithm (with RMSE = 15.62 FNU) was thus deemed adequate to investigate spatial and temporal variations of the turbidity patterns.

The retrieval of SST was performed from TIRS1 band 10 data. The correction of the top of atmosphere brightness temperature *LT* was performed applying the Eq. (2) based on the atmospheric transmission (τ), atmospheric path radiance (*Lu*) and sky radiance (*Ld*). These three parameters were derived by the Atmospheric Correction Parameter Calculator by means of an external link to the NASA website which use MODTRAN radiative transfer model (Barsi et al., 2005, 2014). Per each date the algorithm makes a direct link to this tool (http://atmcorr.gsfc.nasa.gov/), and selects the corresponding standard atmospheric profiles switching during the year the mid-latitude summer and winter. Per each run we honored 30 s time off to avoid the overloading of the web tool.

$$L_{\lambda} = (\tau\varepsilon\, L_T) + (1\text{-}\varepsilon)L_d + L_u \quad (2)$$

τ is the atmospheric transmission, ε is the emissivity of the water (0.98) and L_{λ} is the space-reaching radiance measured by the instrument (Barsi et al., 2005).

Radiance to temperature conversion was then performed using the Planck's Eq. (2).

$$SST(°C) = \frac{K2}{ln\left(\frac{K1}{L_{\lambda}}+1\right)} - 273.15(°C) \quad (3)$$

K1 and K2, respectively the band-specific thermal conversion constants in watts/meter squared * ster * μm and in kelvin.

3.2. Hydrometereological data

Hydrometereological time series were gathered from one hydrologic station and two anemometric stations. Wind direction and speed were measured at the meteorological stations of Acqua Alta Oceanographic Tower (AAOT), located in the NAS, about 16 km off the coast of Venice lagoon, and of Foce Po, between mouth of Tolle and Gnocca (Fig. 1, black triangles), Fig. 4a shows the wind rose diagrams measured in these two points. The river discharge (Fig. 4b) was measured at Pontelagoscuro hydrometric station (Fig. 1, blue circle). These wind diagrams of stations show different sensitivity to the two main wind drivers in this area Bora (from NE) and Scirocco (SW), because of geographical factor (Braga et al., 2017). For being located SE of the delta Foce Po is in fact sheltered from Bora and more exposed to Scirocco and local winds, while AAOT is located in the open sea at the north of delta and is then more affected by Bora.

3.2.1. Hypercubes analysis

Per each scene the procedure provided maps of SST and turbidity along with wind and water discharge measurements from the hydrometereological stations.

The time frame of wind speed and direction data of the investigated stations was selected by considering a temporal window of 36 h prior to the satellite overpass. In the case of discharge, data measured between 10 and 36 h before the overpass were instead considered. This choice permits to account for the typical 10 h time-lag between Pontelagoscuro gauge station and the mouth of Pila, according to Tesi et al. (2011). These three temporal vectors were then pixel-based compared to satellite products.

To calculate the coefficient of variation (CV) of turbidity hypercube and to locate the point of interests for local time series comparison, the turbidity temporal stack was normalized by the averaged water discharge (Q_a) measured at Pontelagoscuro during the interval from 10 to 36 h before the overpass. A descriptive statistic of temporal variation of Q_a-normalized turbidity was built, in particular the mean (μ) and the standard deviation (σ) were computed to calculate a CV map (σ/μ), depicting the dispersion of the turbidity in the temporal range of satellite overpass.

A set of 44 points of interest was selected considering their position related to the river delta and their highest and lowest variability in the study area. These points were identified on the CV Q_a-normalized turbidity maps to identify the location for retrieval of the temporal curves from hypercubes of turbidity and SST. These curves are required to perform the multi-temporal analysis at local targets along the river delta and prodelta area, which are supposed to be representative of the prevailing hydrologic and hydrodynamic conditions. The correlation between time series of SST and Turbidity per each point was performed considering a point into the river as reference.

Correlation patterns with hydrometereological data were evaluated obtaining maps of turbidity sensitivity to wind and water discharge. The Bravais-Pearson's linear correlation (rp) and the Spearman's correlation (rs) methods and the correlation test proposed by Davis (2002) were applied to assess the relation among water discharge, wind speed and turbidity. These two indices describe the strength of link between two variables, Pearson's require the assumption that the relationship between the variables is linear, while Spearman's is a nonparametric (distribution-free) rank statistic that describes the monotonic relationship between two variables without making any assumptions about the frequency distribution of the variables. The statistical significance of the correlation depends on its magnitude and the number of data points used in its computation (Hauke and Kossowski, 2011).

A peak detection algorithm, based on the first derivative analysis of the averaged daily discharge, was applied to identify all the events with discharge higher than 1500 m^3/s defining the local maxima in the time series of the discharge (Fig. 4b). All images acquired within a time window of three days after the identified peaks were selected in order to process only data related to flood events. A correlation analysis of Points Of Interest (POI), considering time series of peak discharge, turbidity and SST was also performed, applying the Spearman's correlation (rs) in addition to the Bravais-Pearson's correlation coefficient (rp) (Bolboaca and Jantschi, 2006).

A geostatistical analysis was performed to determine the spatial dependency of the turbidity datasets per each Landsat image, considering a spatial distance that reduces the scale effects (Van der Meer, 2012). The procedure considered the relation between couples of pixel

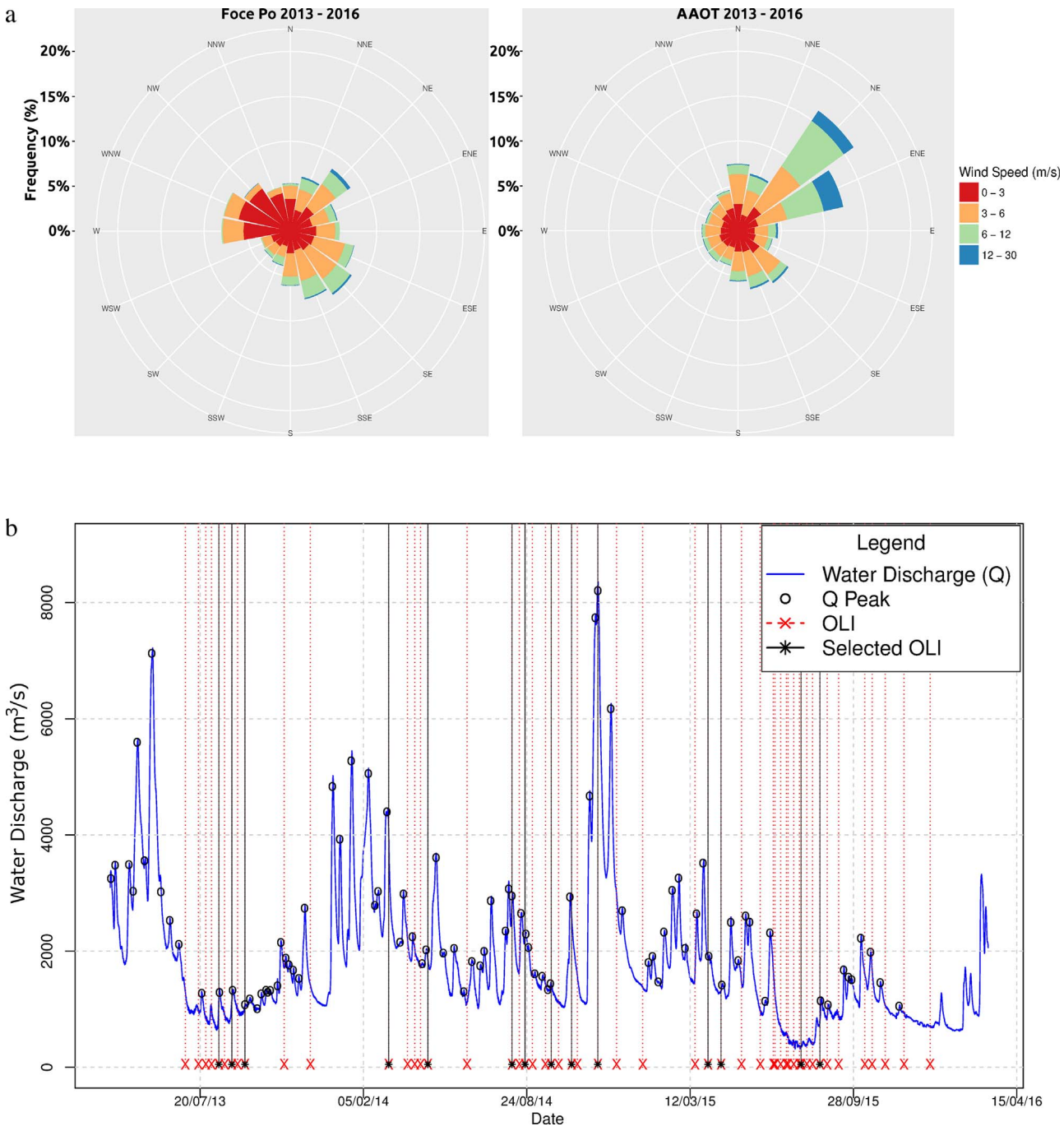

Fig. 4. a) The wind speed and direction measured in Foce Po station and AAOT; b) The water discharge values measured at Pontelagoscuro station. The circles are the peaks detected, the red dot lines and crosses are the Landsat-8 scenes and the black lines are the corresponding peaks with Landsat-8 overpasses. (For interpretation of the references to colour in this figure legend, the reader is referred to the web version of this article).

values Z, located at lag distance h, that is given by the half average squared difference between all such pairs. The semivariance γ(h) for pixel distance is calculated according to Curran and Atkinson (1998):

$$\gamma(h) = \frac{1}{2}E[Z(x) - Z(x+h)]^2 \quad (4)$$

Where Z(x) and Z(x + h) are the random functions describing the property of Z at places separated by h, and E is the mathematical expectation. The larger is the γ(h) the less similar are the pixels (Curran and Atkinson, 1998). The parameter γ(h) is described by semivariogram which defines the spatial dependency of the variable in a covariance stationary process in terms of sill and range. The basic hypothesis is that closer locations have similar values which change for longer distances until they are considered statistically different (autocorrelation range) at sill value (Goovaerts, 1997; Chiles and Delfiner, 1999).

The autofitVariogram (Hiemstra, 2013) and geostatistical routines from R package gstat (Pebesma 2004) were applied to obtain the range and the root mean square of each model and the experimental variogram map.

Per each date of turbidity map the semivariance in every compass direction and distance was calculated in order to identify spatial anisotropy.

The limit of the anisotropy was calculated considering the variance as maximum difference between two pixels to be considered similar.

The directional variograms along the directions of highest and

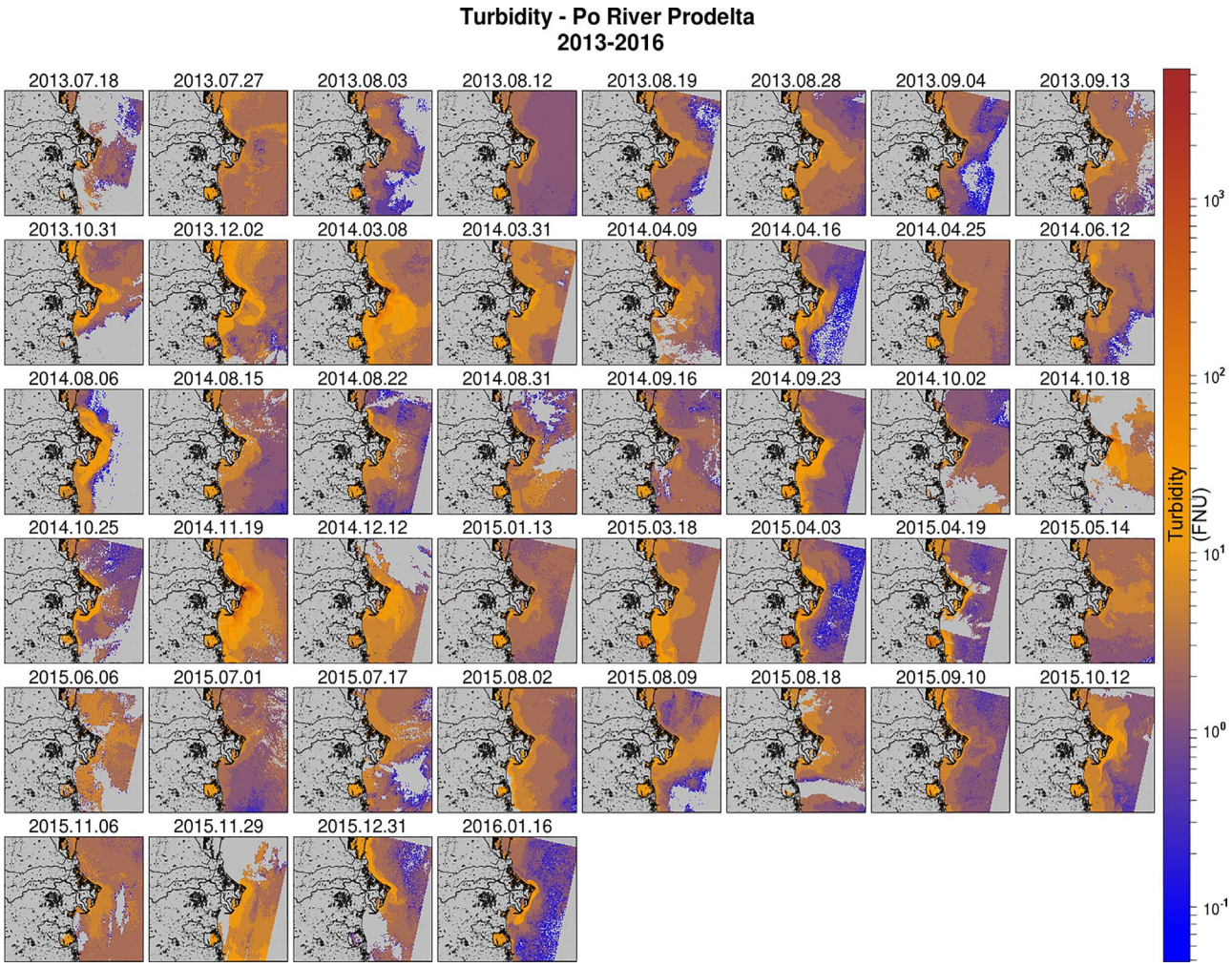

Fig. 5. a) Time series of turbidity map (on a logaritmic scale). b) Time series of Sea Surface Temperature. In black: rivers and coastline; in grey: pixels with no data (e.g. no values, cloud, glint, white cups and land). (For interpretation of the references to colour in this figure legend, the reader is referred to the web version of this article.)

lowest variation of variograms are then collected. These plots are calculated considering the pixels within 35 km from the coastline in the Po River Prodelta and a lag distance of 2300 m thorough which observe directional dependence in semivariograms.

4. Results

The two approaches provide different outputs: the first derived from the punctual analysis of temporal hypercube products, and the second obtained from the spatial statistics.

4.1. Satellite products

The Landsat-8-derived turbidity and SST maps were stacked in two raster datasets (hypercube) for spatial and temporal processing. As observable in the two composites of Fig. 5, turbidity and SST show different patterns and features, both qualitatively (i.e., extent, orientation, shape) and quantitatively (i.e., total amount of suspended sediment, SST gradients), depending on the different hydrologic and meteo-marine conditions. Over the entire dataset, turbidity values ranged from 0.05 to 1500 FNU while SST ranged from 0 to 28 °C.

4.2. Time series derived from the points of interest

The Fig. 6 shows the discharge-normalized coefficient of turbidity variation map, to which the selected 44 points of interest (POI) are overlaid. There is the maximum variability near the distributaries, along the coast and corresponding to river plume with different main directions.

By considering pt3 (located at 5 km upstream of the mouth of Pila) as a reference for the temporal variation of turbidity in the river, the correlation obtained for the other POI is reported in the map of Fig. 6 with a color scale. Pt3 was selected because it is representative of the turbidity values over the most important distributaries and the time series of turbidity in pt3 vs. Pila has correlation (rp) of 0.99. For a given POI, the presence of a higher positive correlation ($rp > 0.85$) indicates that the turbidity variations are quite similar to those found in the river. The points located near Pila and along the southern coast of delta have high rp. This occurs mainly in stations more affected by the buoyant plumes (i.e. Pila and S1), suggesting a major role of discharge, as highlighted by data in Fig. 7, which compares turbidity and discharge time series. Along the NNE direction from Pila there is a fast reduction of POI correlation (NNE mouth in Fig. 6). Low or no correlation indicates that other processes (wind and wave action) are driving suspended sediment pattern in the area (as in NNE mouth Fig. 7).

We also compared SST, but no correlation with turbidity variations in different locations was found considering the whole temporal range. All SST data are correlated ($rp > 0.95$) with temperature variation in pt3, showing that variability is predominantly related to seasonality.

4.2.1. The correlation patterns of turbidity with hydrometereological data

The spatial correlation analysis was performed comparing temporal

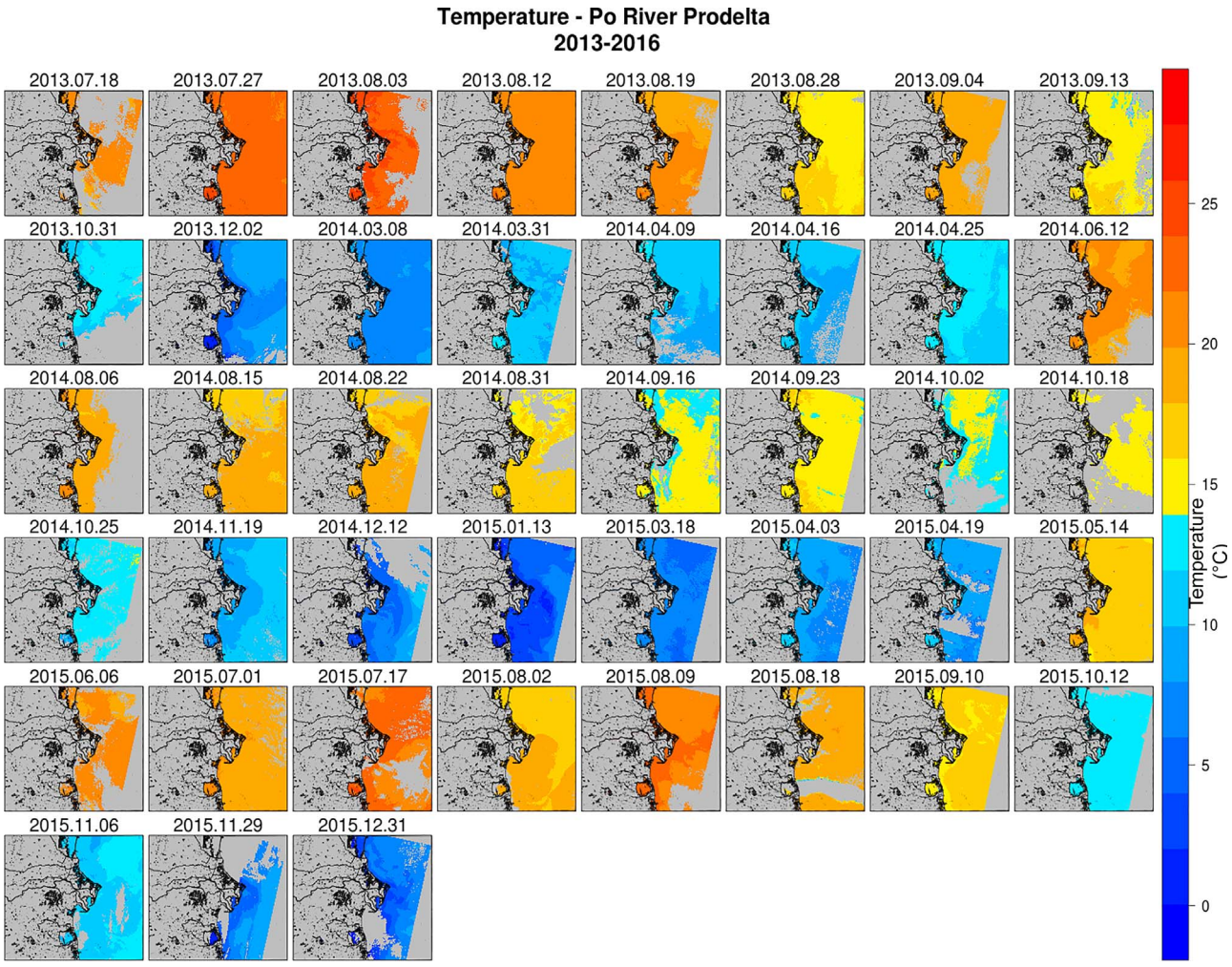

Fig. 5. (*continued*)

curves of each pixel of the hypercube turbidity (Fig. 5) with time series of wind speed measured at Foce Po and AAOT stations and water discharge measured in Pontelagoscuro (Fig. 4). The comparison provided the correlation coefficient maps calculated for these three variables.

In Fig. 8 the correlation map describes the sensitivity of turbidity values to water discharge, in green there are all pixels with a Pearson's correlation greater than 0.75. In this area the water discharge values and turbidity show a linear relationship with each other without considering presence of other hydrodynamic forcing.

The two maps of correlation of wind speed with turbidity in Fig. 9 show interesting phenomena linked to wind forcing effects. The wind measured in two points far more than 50 km have different spatial correlation with turbidity values. The two stations are sensitive to two different wind patterns, as shown by the wind rose diagrams in Fig. 4a, defining two different wind stiles, more sensitive to Bora in the case of AAOT while in the case of Foce Po, more related to local effects. The different spatial pattern of correlation of these two maps underlines the different wind measurements and the effects on the NAS basin.

Indeed, Fig. 9a shows that the wind speed measured in AAOT has correlation with turbidity in the north of prodelta area until the Venice lagoon (dark red area). Due to local effects of wind in Foce Po station the measurements were not necessary similar to AAOT, consequently the correlation coefficient maps calculated are different. Considering Fig. 9b there is a correlation between the wind speed in Foce Po and the turbidity values along the coast from Maistra to Bellocchio.

4.3. Peak detection

The peak analysis of the water discharge measured in Pontelagoscuro selected the Landsat scenes near to water discharge peak during flooding events. We therefore considered the local maxima of the discharge and selected all the scene overpasses within 3 days after the flood.

The comparison of time series of SST, turbidity of the POI and water discharge, in this case resulted in a better correlation, showing that in flood conditions there are higher statistical links with turbidity and temperature variation (Table 1). Moreover, the wind speed had no statistical link underlining the lower or negligible importance of this variable in these cases.

As showed in Table 1, near the Po River delta the water discharge caused a temperature reduction in the Pila area with an inverse correlation of rs = −0.62 and a confidence of 90%, while it has a positive correlation with turbidity of rp = 0.83 with a confidence of 99%. The variation of temperature in Pila is directly correlated to the temperature variation in Tolle with rp = 0.89 and is inversely correlated to the variation of turbidity in Tolle with rs = −0.72.

Some couples have different correlation values, this is due to their respective calculation which have different assumption, if there are non-linear correlation the Spearman's correlation will be higher as in the case of thermal values of Pila with other points.

Table 1 Correlation intra-parameter and inter-parameter between water discharge (Qavg), Turbidity and SST time series of Po tributaries, pt3 and S1with relative confidence > 90% (*) and > 95% (**). In bold

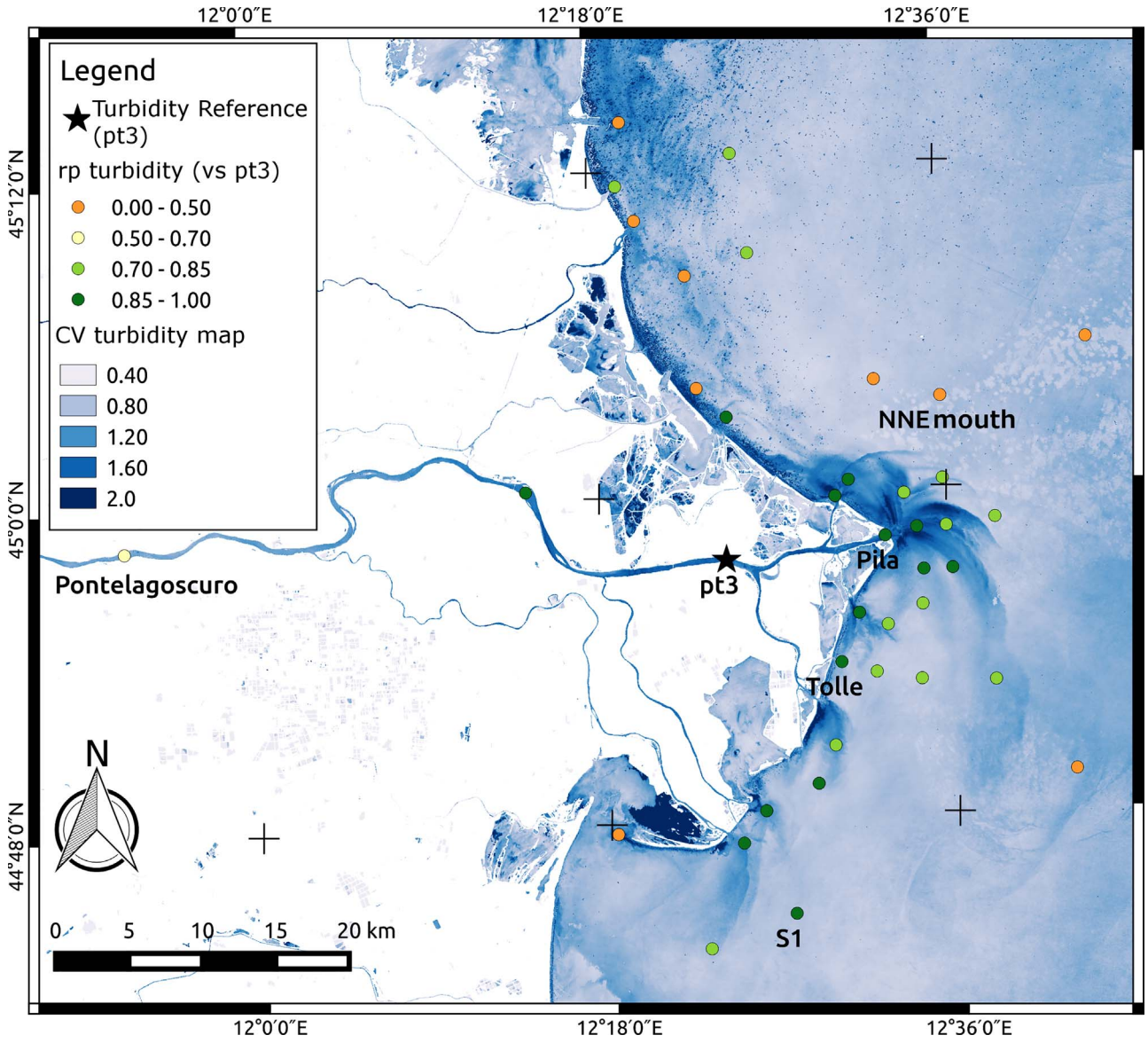

Fig. 6. Coefficient of turbidity variation (σ/μ) (CV) map in the study area. The dots represent the correlation (rp) of turbidity values retrieved in each location with turbidity in pt3.

relation with correlation > |0.6|

The Fig. 10 shows the point map of correlation among SST retrieved in pt3 with turbidity values in the POI. The points far from the coast have no statistical link. Considering these two results, the lower statistical correlation between temperature and turbidity with water discharge underlines that this is not the unique driver of temperature variation.

4.4. The geostatistical patterns

The variogram maps describe the spatial variability of turbidity in every compass direction per each date supporting the identification of spatial anisotropy structures in the values distributions. This analysis provided some interesting results in extreme events such as during wind blowing (as Bora, Scirocco) and floods. The Fig. 11 shows how the spatial variability of turbidity changes in different forcing conditions, the anisotropy ellipses show the spatial patterns provided by analysis of turbidity variation. The limit of autocorrelation was based on the analysis of directional variograms. Indeed, the variograms along the main axis of variability and its perpendicular axis show the maximum distance where two pixel values are no more spatially correlated. In Fig. 11 – 2014/09/23 the Bora event is the main driver causing wind resuspension (Braga et al., 2017), the a priori variance of turbidity (dashed lines in the directional variogram plot) is lower than the other two cases, this means that the turbidity values have a lower range of variability, the maximum autocorrelation distance is reached at N20 with a distance of 33 km. In Fig. 11 – 2014/11/19 during "flood dominant" phase the pixels show a higher variability range and along W-E direction have low variability with an autocorrelation distance of 25 km, while the minor axis is 15 km. Finally in Fig. 11 – 2015/04/03 there is an example of Scirocco (Southeasterly) wind event during which the sediments changes along the direction N150 stabilizing the variogram near the a priori variance. The nugget effect is very high in this last case underling that neighbor pixels have a higher level of variability no-spatially correlated. Then the direction N60 reduce the variation rate with lag distance after 30 km with high variance values, representing a trend, fining upward.

5. Discussions

The results compare the two measured hydrodynamic forcing, the water discharge and the wind, with simultaneous optical and thermal

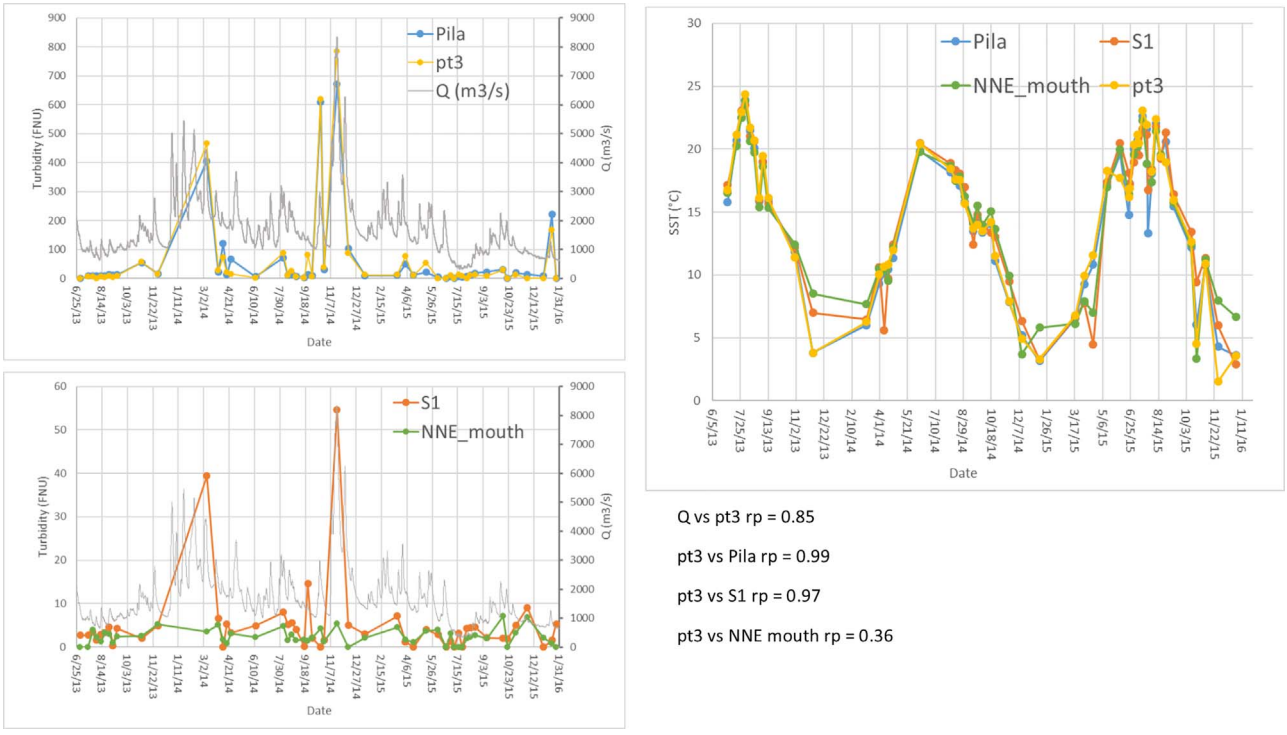

Fig. 7. Temporal variation of turbidity (on the left) and SST (on the topright) at pt3, Pila, NNE mouth, S1. Water discharge measured in Pontelagoscuro Station is plotted as grey line. The rp values bottom right are: the correlation (rp) of turbidity of pt3 with water discharge (Q) and Pila, NNE mouth, S1 turbidities. (For interpretation of the references to colour in this figure legend, the reader is referred to the web version of this article.)

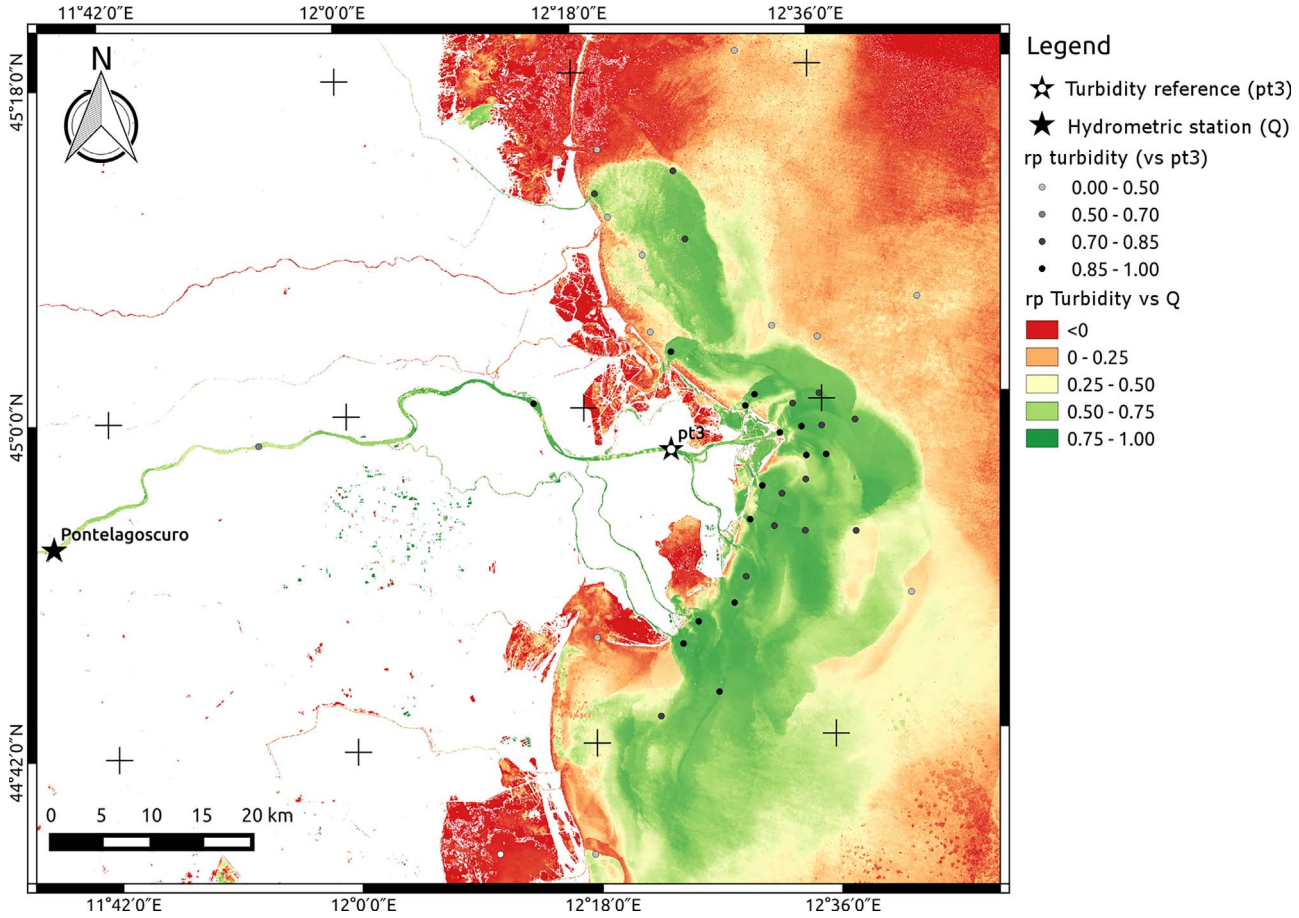

Fig. 8. Correlation between water discharge and turbidity values in the study area. In gray scale the correlation of turbidity values pt3 vs. POI. (For interpretation of the references to colour in this figure legend, the reader is referred to the web version of this article.)

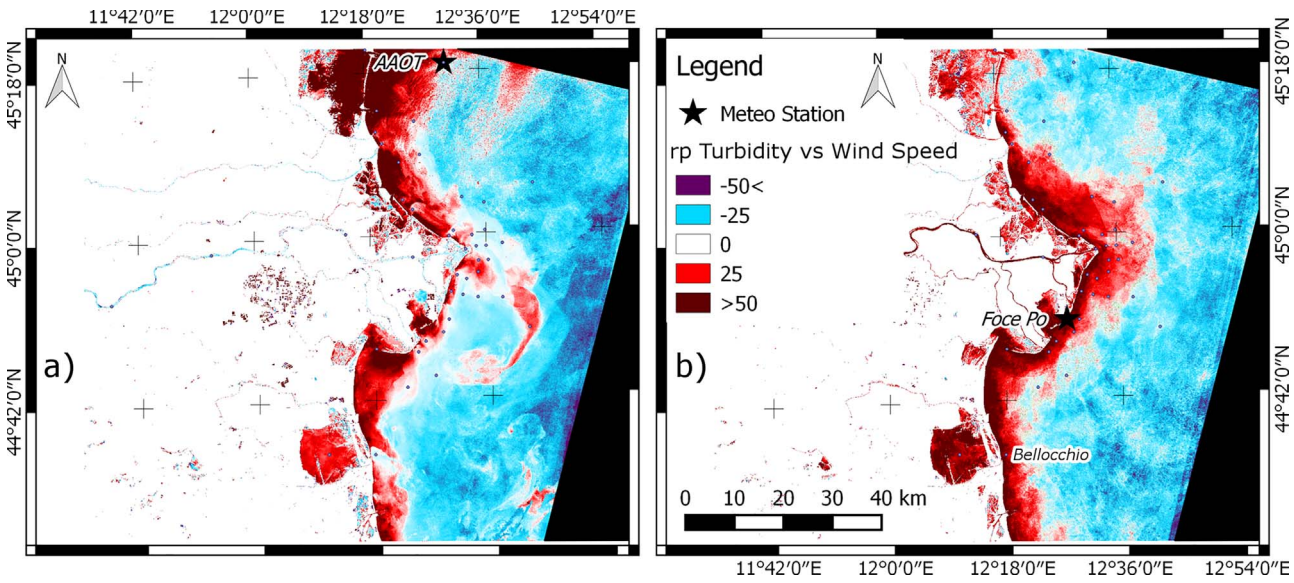

Fig. 9. Correlation (rp) map of Turbidity vs Wind Speed measured in the two meteo-station of AAOT (a) and of Foce Po (b). (For interpretation of the references to colour in this figure legend, the reader is referred to the web version of this article.)

satellite data obtaining the highest sensitive area to the measured forcings (Figs. 6,8 and 9), the link between turbidity, SST and water discharge during the floods (Table 1) and finally the geometrical patterns of turbidity variability (Fig. 11). This information is important for determining stresses on the ecosystem since the high concentrations of suspended matter through the river plumes and wave-driven resuspension increase the turbidity and decrease light penetration conditioning the growth of aquatic vegetation and consequently the ecology.

Landsat-8 data confirmed their capability to analyse the Po River prodelta in terms of spatial analysis and statistical correlation with hydrometereological data at the submesoscale enlarging the

Table 1
Correlation intra-parameter and inter-parameter between water discharge (Qavg), Turbidity and SST time series of Po tributaries, pt3 and S1with relative confidence > 90% (*) and > 95% (**). In bold relation with correlation > |**0.6**|.

SST (°)

	Qavg	Maistra	Pila	Tolle	Gnocca	Goro	pt3
Maistra	**rp = −0.56***						
Pila	**rp = −0.64****	**rp = 0.99****					
Tolle	rp = −0.49	**rp = 0.91****	**rp = 0.89****				
Gnocca	rp = −0.42	**rp = 0.92****	**rp = 0.88****	**rp = 0.86****			
Goro	**rs = −0.54***	**rp = 0.97****	**rp = 0.95****	**rp = 0.88****	**rp = 0.91****		
pt3	**rp = −0.65****	**rp = 0.99****	**rp = 0.99****	**rp = 0.89****	**rp = 0.88****	**rp = 0.94****	
S1	rs = −0.49	**rp = 0.97****	**rs = 0.96****	**rp = 0.87****	**rp = 0.90***	**rp = 0.98****	**rs = 0.96****

Turbidity (FNU)

	Qavg	Maistra	Pila	Tolle	Gnocca	Goro	pt3
Maistra	**rp = 0.92****						
Pila	**rp = 0.83****	**rp = 0.89****					
Tolle	**rp = 0.97****	**rp = 0.96****	**rp = 0.97****				
Gnocca	**rp = 0.97****	**rp = 0.94****	**rp = 0.98****	**rp = 1.00****			
Goro	**rp = 0.96****	**rp = 0.86****	**rp = 0.99****	**rp = 0.96****	**rp = 0.98****		
pt3	**rp = 0.88****	**rp = 0.87****	**rp = 0.85****	**rp = 0.88****	**rp = 0.81****	**rp = 0.82****	
S1	**rp = 0.93****	**rp = 0.83***	**rp = 0.97****	**rp = 0.94****	**rp = 0.96****	**rp = 0.98****	**rp = 0.98****

	SST (°)							
	vs	Maistra	Pila	Tolle	Gnocca	Goro	pt3	S1
Turbidity (FNU)	Maistra	**rs = −0.66***	**rs = −0.72****	rs = −0.51*	rs = −0.48	**rs = −0.66****	**rs = −0.71****	**rs = −0.64***
	Pila	rp = −0.49	rp = −0.53**	rs = −0.45	rp = −0.41	rp = −0.52**	rp = −0.55*	rs = −0.31
	Tolle	**rs = −0.68****	**rs = −0.72****	rs = −0.60*	rp = −0.42	rs = −0.57*	**rs = −0.68****	rs = −0.55*
	Gnocca	**rs = −0.79****	**rs = −0.85****	**rs = −0.68***	**rs = −0.74****	**rs = −0.76****	**rs = −0.85****	**rs = −0.75***
	Goro	**rs = −0.69****	**rs = -0.73****	rp = −0.59*	rs = −0.57**	**rs = −0.67****	**rs = −0.74****	**rs = −0.64***
	pt3	rp = −0.56**	rp = −0.55**	rp = −0.45	p = −0.44	rp = −0.52*	rp = 0.58*	rs = −0.41
	S1	**rp = −0.63***	**rp = −0.67**	rp = −0.58	rp = −0.53	**rp = −0.63***	**rp = −0.69***	rp = −0.58

* = confidence at 90%, ** = confidence > 95%.

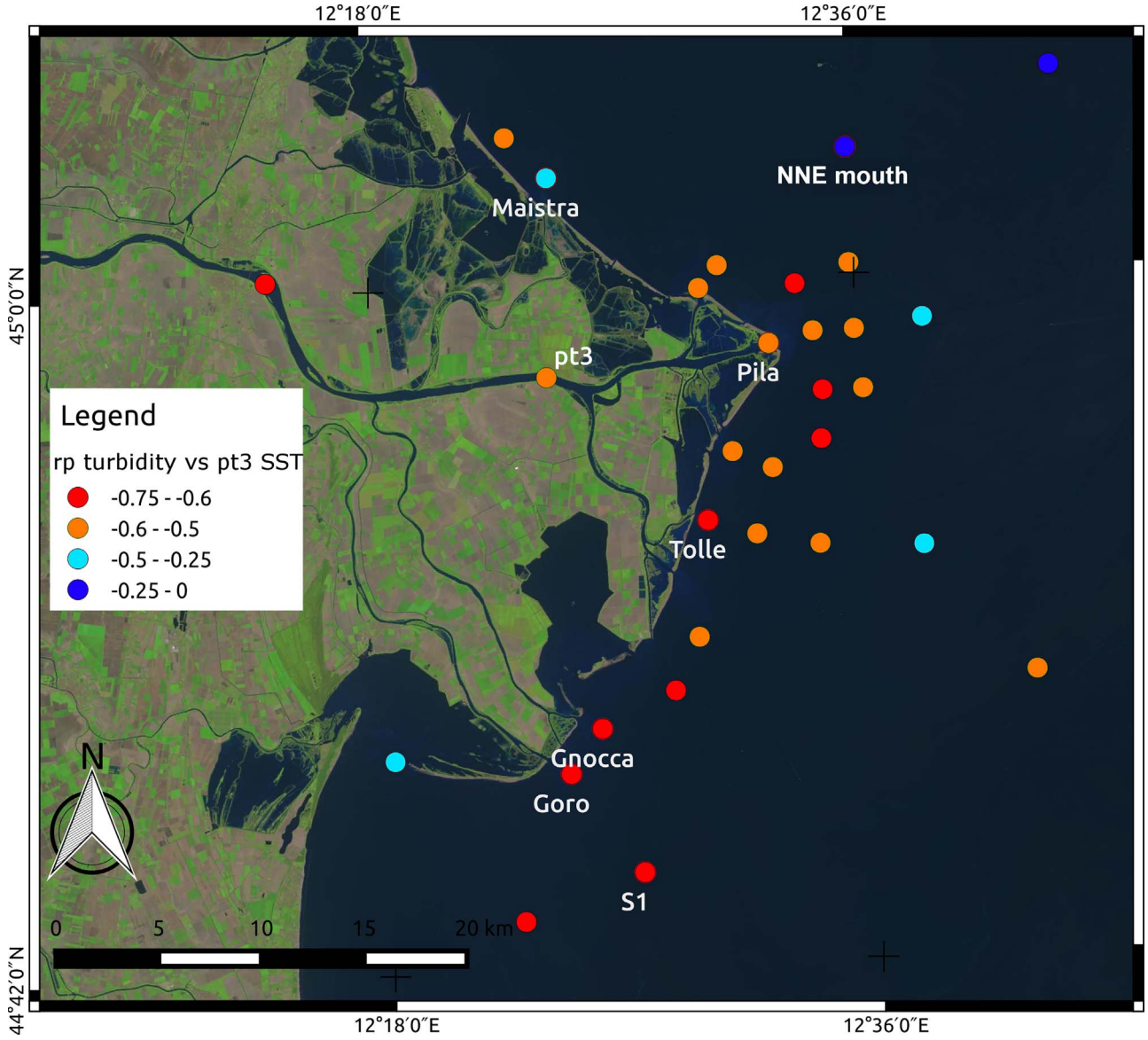

Fig. 10. Correlation (rp) among SST in pt3 and turbidity values in the POI. (For interpretation of the references to colour in this figure legend, the reader is referred to the web version of this article.)

environmental analysis of Po river plumes provided by Braga et al. (2017) and Brando et al. (2015) with other products.

Build upon and extended the previous results, the processing chain adopts two main processing approaches, one based on punctual extraction of time series of satellite products, another worked on entire scene. By the first a series of points of interest (POI) were derived in order to focus on the areas with highest variability linked to strong changes due to natural forcings. The second approach provided map of correlation and geostatistical analysis which provided general information over the study area.

Pila confirms its important role as main distributary of Po River, and the investigated parameters are in correlation with those found in the adjacent coastal zones and tributaries. Other factors such as salinity may be considered for a comprehensive interpretation of the hydrological forcings as demonstrated by Brando et al. (2015) and Marini et al. (2008), but it is beyond the scope of this paper. The maps of correlation of turbidity and water discharge show as the Po river plume in flood conditions affects sediment distribution in the prodelta (values $rp > 0.75$). Based on the sole turbidity, the river plume area extends southward, parallel to the coastline, to a maximum distance of 35 km, while reaching an offshore distance of 15 km. The extent of the area impacted by river plume is also evident in the geostatistical pattern where the autocorrelation distance was within this order of magnitude. Beyond these limits and in other directions, the spatial distribution of the turbidity is more affected by dilution trends and other forcings such as wind, waves and currents.

The choice of the temporal window of hydro-meteorological data to be considered is quite challenging as satellite images reflect instantaneous situation created by the interaction of different forcings, each acting on a proper time frame and spatial extent, during the previous period. We then selected a temporal window of 36 h prior to the satellite overpass for wind conditions because most wind effects were registered within this interval, as showed by Braga et al. (2017).

A higher overpass frequency of satellite data would improve the characterization of the river plume and its evolution. The temporal window of three days to select images related to discharge peaks provides in fact a limited number of events (Fig. 4b). MERIS data were used in this area to perform a temporal analysis of driver effect applying the empirical orthogonal function EOF (Filipponi et al., 2014) obtaining interesting results but at coarser spatial resolution. Landsat-8 data

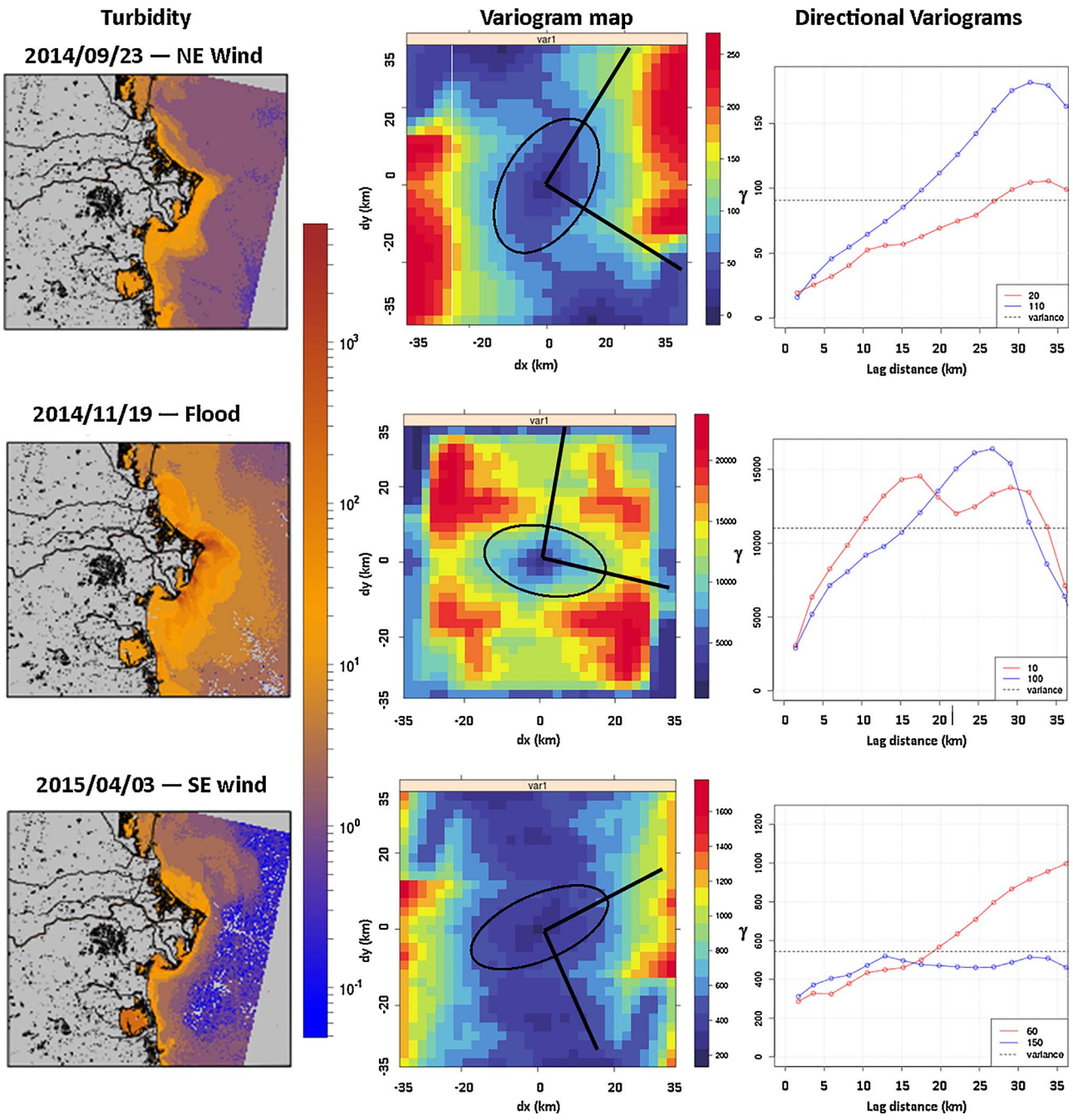

Fig. 11. On the left the turbidity maps in different forcing conditions (color ramp of turbidity in log scale). In the middle column the corresponding variogram maps of turbidity. The dx and dy axes are separation distances between couples of pixels along E-W and N-S directions, respectively. Each grid cell is the semivariance contribution of each point pair at lag (x, y) = h being the two-dimensional coordinates of the separation vector. The center of the variogram map (0; 0) is the origin of the variogram map for every direction, and h is geographical distance among pixels. On the right the variograms of two major and minor axis of variability. (For interpretation of the references to colour in this figure legend, the reader is referred to the web version of this article.)

might not be adequate for capturing multi-temporal analysis of inter-annual and seasonal variability in the NAS, as demonstrated by the peak detection analysis. Indeed, several peaks were not intersected (Fig. 4b) and the analysis was performed on a limited number of scenes, yet obtaining interesting results in terms of higher and significant correlations.

During a flood, riverine water is colder and with higher turbidity than NAS, for this reason we consider turbidity and in some cases SST two proxies of floods. However, the difference of temperature between Po River and NAS is seasonal, while the variation of turbidity is driven by riverine discharge peaks or resuspension. Brando et al. (2015) showed how they change between different rivers in the NAS during a flood event while in our paper we are focusing on the temporal variation over Po River prodelta. Focusing on the Landsat images corresponding to the events identified by discharge peak detection (Table 1), the comparison between SST and turbidity shows good statistical correlations in some points of interest, while the low correlation with wind suggests that the wind effect is secondary to river discharge. The Spearman's coefficients of SST retrieved for Pila versus the values obtained for Gnocca and Goro highlighted that there are monotonic correlations among these points (Table 1). Consequently, during flood events, these areas are characterized by a similar behavior. SST in pt3 compared to the turbidity values in Pila, Gnocca and S1 has high correlation while it is low in the external points, we interpret this as an

evidence that the plumes tend to extend from Pila southeastward near the coast, probably due to WACC as shown by Braga et al. (2017) and Filipponi et al. (2014). Comparing singularly the turbidity and SST time series of POI, the Pearson's correlation is the most relevant in the definition of statistical link. This is probably related to the distance between POI which mainly drives the parameter variability. Therefore, cross-comparing the SST and Turbidity of POI time series, the Spearman statistical correlation is more relevant. The non-linear correlation is, as expected, related to the presence of more factors playing in the spatial and interparametric variability. The monotonic correlation showed by Spearman's coefficient underlines the effect of water discharge in the SST variation in the coastal zone, but the weak correlation highlights also that there are other phenomena that need to be considered. So the sediment transport and temperature have physical forcing regimes affecting their variability both on spatial and temporal scales. Focusing only on water discharge peaks, the main driver of turbidity is the water discharge and the POI were stronger correlated to this parameter than the temperature. As demonstrated by Brando et al. (2015), satellite-derived turbidity and SST can be useful to describe flood events, defining the plume morphology and the dilution pathways. However, the availability of other ancillary data could support the interpretation of the mixing processes in the prodelta area; for instance, salinity, which can be provided by numerical modelling (Falcieri et al., 2014) or in situ measurements (Boldrin et al., 2005).

The geostatistical analysis of satellite-derived turbidity maps (Fig. 11) identify three main types of spatial patterns in relation to the different forcings (river discharge, Bora or Scirocco winds), defining spatial anisotropy with axis and orientations as function of the natural drivers. In case of small plumes confined to coastal areas, typical of low discharges and/or Bora wind event (2013/09/23 − Fig. 11) the range of turbidity is shorter and the main axis of the anisotropy ellipse follow direction N20, with a low eccentricity. In the case of wider plumes extending into the basin, as typical of flood events (2014/11/19 − Fig. 11) and/or Scirocco winds (2015/04/03 − Fig. 11), high turbidity values are generally found over the prodelta area. In the first case the anisotropy follows the W-E direction with a main axis of 30 km and eccentricity higher than in the Bora event. In the case of Scirocco event, a strong turbidity gradient at small scale can be observed. This situation is characterized by high nugget values and the variogram shows a trend model along direction N60. The interaction of wind and water discharge determines ellipses of anisotropy characterized by long autocorrelation distance, although the mixing and the rotation due to Coriolis force may affect the geostatistical analysis.

6. Conclusions

Understanding the spatial and temporal variability of the Po river plume is of primary importance for the study of the Adriatic Sea basin and its evolution. By focusing on the Po River delta, this research tested a procedure based on Landsat-8-derived products to characterize river plume dispersion using statistical tools for investigating the effects of discharge and meteo-marine forcings on sediment transport patterns in prodelta areas. The pixel-based spatial correlation analysis, based on the comparison of turbidity and SST hypercubes with in situ data, confirmed the relationship between turbidity and water discharge in the area more affected by the buoyant plumes and along the southern coast of Po River delta. An inverse correlation between turbidity and SST was observed focusing the analysis on flood events. As shown by the results of this test, the geostatistical analysis allows to determine the spatial dependency of the turbidity datasets per each satellite image, identifying different spatial anisotropy structures of turbidity in response to ambient conditions (i.e. strong Bora or Scirocco winds, floods).

The results obtained provide new perspectives for the analysis of transitional environments through satellite data, such as turbidity and SST, identifying their spatial and temporal distributions in relation to river and wind regimes in the prodelta and adjacent coastal zone.

Although limited by low revisit frequency of Landsat-8 overpasses, the described methodology is a very promising and robust processing technique for time series analysis suitable for handling large amounts of data. This will open chances for a considerable improvement of multi-temporal analysis of interannual and seasonal variability of river plumes in case Sentinel-2A and −2B, recently launched by ESA, are used. The turbidity analysis by the Landsat-8 has shown its potential for synoptic observations of dynamic environments that could be further improved by the application of Sentinel-2 data, in terms of spatial and temporal resolution. Reducing the revisit time, these data will provide significant advantages in the observation of short time scale processes like those related to floods and sea storm events. For moderate to low river flow, the characterization of buoyant plume with satellite-derived products can benefit from the integration with in situ measurements and hydrodynamic models, providing a better description of horizontal and vertical mixing processes.

Future research work will be focused on the processing methodology, implementing new statistical tools for spatio-temporal analysis, such as empirical orthogonal function to better investigate the temporal variations of these environments.

Being based on open source software and free satellite data, this processing chain and its eventual further improvements could become a tool of general use for monitoring river plumes and the associated load of sediments and contaminants and for the management of estuarine, coastal and open sea waters, also supporting directives for the conservation of maritime ecosystems.

Acknowledgments

Landsat-8 data are available from the U.S. Geological Survey. We are grateful to NASA and Dr. Julia Barsi for WebTool and support. The authors thank the Italian Institute for Environmental Protection and Research (ISPRA) for providing wind speed and direction. We are grateful to RBINS for making ACOLITE publicly and freely available. We are grateful to the Environmental Protection Agency of Region of Emilia Romagna for water discharge data at Pontelagoscuro. This study was co-funded by the Italian Space Agency (ASI) (CLAM-PHYM project, contract no. I/015/11/0) and EU FP7 INFORM (Grant No. 606865). We acknowledged the funding from RITMARE Flagship Project and the European Union (FP7-People Co-funding of Regional, National and International Programmes, GA no. 600407). We also wish to thank the three anonymous reviewers for their constructive comments, which helped to strengthen this study.

References

Aldabash, M.D., Balik, F., 2016. Analysis of multi temporal satellite imagery for total suspended sediments in a wave-active coastal area-gaza strip coastal water, Palestine. Int. J. Environ. Geoinform. 3 (1).

Artegiani, A., Paschini, E., Russo, A., Bregant, D., Raicich, F., Pinardi, N., 1997. The adriatic sea general circulation. part II: baroclinic circulation structure. J. Phys. Oceanogr. 27 (8), 1515–1532.

Barsi, J.A., Schott, J.R., Hook, S.J., Raqueno, N.G., Markham, B.L., Radocinski, R.G., 2014. Landsat-8 thermal infrared sensor (TIRS) vicarious radiometric calibration. Remote Sens. 6 (11), 11607.

Barsi, J.A., Schott, J.R., Palluconi, F.D., Hook, S.J., 2005. Validation of a web-based atmospheric correction tool for single thermal band instruments. Opt. Photon. (58820E).

Bever, A.J., Harris, C.K., Sherwood, C.R., Signell, R.P., 2009. Deposition and flux of sediment from the Po river, Italy: an idealized and wintertime numerical modeling study. Mar. Geol. 260 (1), 69–80.

Bivand, R.S., Pebesma, E., Gomez-Rubio, V., 2013. Spatial Data Import and Export. In Applied Spatial Data Analysis with R. Springer, pp. 83–125.

Bolboaca, S.D., Jantschi, L., 2006. Pearson versus spearman, kendall's tau correlation analysis on structure-activity relationships of biologic active compounds. Leonardo J. Sci. 5 (9), 179–200.

Boldrin, A., Langone, L., Miserocchi, S., Turchetto, M., Acri, F., 2005. Po River plume on the Adriatic continental shelf: dispersion and sedimentation of dissolved and suspended matter during different river discharge rates. Mar. Geol. 222, 135–158.

Bonamano, S., Piermattei, V., Madonia, A., Paladini de Mendoza, F., Pierattini, A.,

Martellucci, R., Stefanì, C., Zappalà, G., Caruso, G., Marcelli, M., 2016. The Civitavecchia Coastal Environment Monitoring System (C-CEMS): a new tool to analyze the conflicts between coastal pressures and sensitivity areas. Ocean Sci. 100, 2016. http://dx.doi.org/10.5194/os-12-87-2016.
Braga, F., Zaggia, L., Bellafiore, D., Bresciani, M., Giardino, C., Lorenzetti, G., Maicu, F., Manzo, C., Riminucci, F., Ravaioli, Brando, V.E., 2017. Mapping turbidity patterns in the Po river prodelta using multi-temporal Landsat 8 imagery. Estuar. Coast. Mar. Sci. 198, 555–567.
Brando, V.E., Braga, F., Zaggia, L., Giardino, C., Bresciani, M., Matta, E., Bellafiore, D., Ferrarin, C., Maicu, F., Benetazzo, A., Bonaldo, D., Falcieri, F.M., Coluccelli, A., Russo, A., Carniel, S., 2015. High-resolution satellite turbidity and sea surface temperature observations of river plume interactions during a significant flood event. Ocean Sci. 11 (6), 909–920.
Brodie, J., Schroeder, T., Rohde, K., Faithful, J., Masters, B., Dekker, A., Brando, V., Maughan, M., 2010. Dispersal of suspended sediments and nutrients in the Great Barrier Reef lagoon during river-discharge events: conclusions from satellite remote sensing and concurrent flood-plume sampling. Mar. Freshwater Res. 61 (6), 651–664.
Cannizzaro, J.P., Carlson Jr, PR, Yarbro, L.A., Hu, C., 2013. Optical variability along a river plume gradient: implications for management and remote sensing. Estuar. Coast. Mar. Sci. 131, 149–161.
Chen, S., Huang, W., Chen, W., Wang, H., 2011. Remote sensing analysis of rainstorm effects on sediment concentrations in Apalachicola Bay, USA. Ecol. Inform. 6 (2), 147–155.
Chiles, J.P., Delfiner, P., 1999. Geostatistics: Modeling Spatial Uncertainty. Wiley, New York; Chichester.
Cristina, S., Icely, J., Goela, P.C., Del Valls, T.A., Newton, A., 2015. Using remote sensing as a support to the implementation of the European Marine Strategy Framework Directive in SW Portugal. Cont. Shelf Res. 108, 169–177.
Curran, P.J., Atkinson, P.M., 1998. Geostatistics and remote sensing. Prog. Phys. Geogr. 22 (1), 61–78.
Davidson Arnott, R., 2010. Introduction to Coastal Processes and Geomorphology. Cambridge University Press.
Davis, J.C., 2002. Statistics and Data Analysis in Geology, 3rd ed. John Wiley and Sons, Inc., New York.
Dogliotti, A.I., Ruddick, K., Guerrero, R., 2016. Seasonal and inter-annual turbidity variability in the Río de la Plata from 15 years of MODIS: El Niño dilution effect. Estuar. Coast. Mar. Sci. 182 (Part A), 27–39.
Dogliotti, A., Ruddick, K., Nechad, B., Doxaran, D., Knaeps, E., 2015. A single algorithm to retrieve turbidity from remotely-sensed data in all coastal and estuarine waters. Remote Sens. Environ. 156, 157–168.
Doxaran, D., Ehn, J., Bélanger, S., Matsuoka, A., Hooker, S., Babin, M., 2012. Optical characterisation of suspended particles in the Mackenzie River plume (Canadian Arctic Ocean) and implications for ocean colour remote sensing. Biogeosciences 9 (8), 3213–3229.
Falcieri, F.M., Benetazzo, A., Sclavo, M., Russo, A., Carniel, S., 2014. Po River plume pattern variability investigated from model data. Cont. Shelf Res. 87, 84–95.
Falcini, F., Khan, N.S., Macelloni, L., Horton, B.P., Lutken, C.B., McKee, K.L., Santoleri, R., Colella, S., Li, C., Volpe, G., D'Emidio, M., Salusti, A., Jerolmacke, D.J., 2012. Linking the historic 2011 Mississippi River flood to coastal wetland sedimentation. Nat. Geosci. 5 (11), 803–807.
Filipponi, F., Taramelli, A., Zucca, F., Valentini, E., Serafy, G.Y., 2015. Ten-years sediment dynamics in Northern Adriatic Sea investigated through optical remote sensing observations. 2015 IEEE International Geoscience and Remote Sensing Symposium (IGARSS) 2265–2268.
Filipponi, F., Valentini, E., Liberti, L., Zucca, F., Taramelli, A., 2014. 2014. Generation of gridded Ocean Color products from MERIS: an efficient processing chain. IEEE GOLD Remote Sensing Conference.
Franz, B.A., Bailey, S.W., Kuring, N., Werdell, P.J., 2015. Ocean color measurements with the Operational Land Imager on Landsat-8: implementation and evaluation in SeaDAS. J. Appl. Remote. Sens. 9, 096070.
Friedrichs, C.T., Scully, M.E., 2007. Modeling deposition by wave-supported gravity flows on the Po River prodelta: from seasonal floods to prograding clinoforms. Cont. Shelf Res. 27 (3), 322–337.
Gernez, P., Lafon, V., Lerouxel, A., Curti, C., Lubac, B., Cerisier, S., Barillé, L., 2015. Toward sentinel-2 high resolution remote sensing of suspended particulate matter in very turbid waters: SPOT4 (Take5) experiment in the loire and gironde estuaries. Remote Sens. 7 (8), 9507. http://dx.doi.org/10.3390/rs70809507.
Geyer, W., Hill, P., Kineke, G., 2004. The transport, transformation and dispersal of sediment by buoyant coastal flows. Cont. Shelf Res. 24, 927–949.
Gippel, C.J., 1995. Potential of turbidity monitoring for measuring the transport of suspended solids in streams. Hydrol. Process. 9 (1), 83–97.
Goovaerts, P., 1997. Geostatistics for Natural Resources Evaluation. Oxford University Press, New York; Oxford.
Hauke, J., Kossowski, T., 2011. Comparison of values of Pearson's and Spearman's correlation coefficients on the same sets of data. Quaestiones Geographicae 30 (2), 87–93.
Hetland, R.D., 2005. Relating river plume structure to vertical mixing. J. Phys. Oceanogr. 35 (9), 1667–1688.
Hiemstra, P., 2013. Package 'automap'. Compare 105, 10.
Hijmans, R.J., 2014. Geographic Data Analysis and Modeling [R Package Raster Version 2.5-8].
Horner-Devine, A.R., Hetland, R.D., MacDonald, D.G., 2015. Mixing and transport in coastal river plumes. Annual Review of Fluid Mechanics 47, 569–594.
Irons, J.R., Dwyer, J.L., Barsi, J.A., 2012. The next Landsat satellite: the Landsat data continuity mission. Remote Sens. Environ. 122, 11–21.
Kirk, J.T., 1994. Light and Photosynthesis in Aquatic Ecosystems. Cambridge university press.
Kourafalou, V.H., 2001. River plume development in semi-enclosed mediterranean regions: north adriatic sea and northwestern aegean sea. J. Mar. Syst. 30 (3), 181–205.
Lavrova, O.Y., Soloviev, D.M., Strochkov, M.A., Bocharova, T.Y., Kashnitsky, A.V., 2016. River plumes investigation using sentinel-2A MSI and landsat-8 OLI data. Proc. SPIE. http://dx.doi.org/10.1117/12.2241312. 9999, p. 99990G-99990G-12.
Lee, Z., Shang, S., Lin, G., Chen, J., Doxaran, D., 2016a. On the modeling of hyperspectral remote-sensing reflectance of high-sediment-load waters in the visible to shortwave-infrared domain. Appl. Opt. 55, 1738–1750.
Lee, Z., Shang, S., Qi, L., Yan, J., Lin, G., 2016b. A semi-analytical scheme to estimate Secchi-disk depth from Landsat-8 measurements. Remote Sens. Environ. 177, 101–106.
Lymburner, L., Botha, E., Hestir, E., Anstee, J., Sagar, S., Dekker, A., Maltus, T., 2016. Landsat 8: Providing continuity and increased precision for measuring multi-decadal time series of total suspended matter. Remote Sens. Environ. 185, 108–118. http://dx.doi.org/10.1016/j.rse.2016.04.011.
Ma, Y., Wu, H., Wang, L., Huang, B., Ranjan, R., Zomaya, A., Jie, W., 2015. Remote sensing big data computing: challenges and opportunities. Future Gener. Comput. Syst. 51, 47–60. http://dx.doi.org/10.1016/j.future.2014.10.029.
Malone, T.C., Di Giacomo, P.M., Goncalves, E., Knap, A.H., Talaue-McManus, L., de Mora, S., Muelbert, J., 2014. Enhancing the Global Ocean Observing System to meet evidence based needs for the ecosystem-based management of coastal ecosystem services. Nat. Resour. Forum 38 (3), 168–181. http://dx.doi.org/10.1111/1477-8947.12045.
Marini, M., Jones, B.H., Campanelli, A., Grilli, F., Lee, C.M., 2008. Seasonal variability and Po river plume influence on biochemical properties along western Adriatic coast. J. Geophys. Res.: Oceans 113, C5.
Milliman, J.D., Farnsworth, K.L., 2013. River Discharge to the Coastal Ocean: a Global Synthesis. Cambridge University Press.
Nechad, B., Alvera-Azcaràte, A., Ruddick, K., Greenwood, N., 2011. Reconstruction of MODIS total suspended matter time series maps by DINEOF and validation with autonomous platform data. Ocean Dyn. 61 (8), 1205–1214.
Nechad, B., Ruddick, K., Park, Y., 2010. Calibration and validation of a generic multisensor algorithm for mapping of total suspended matter in turbid waters. Remote Sens. Environ. 114 (4), 854–866.
Nof, D., Pichevin, T., 2001. The ballooning of outflows. J. Phys. Oceanogr. 31 (10), 3045–3058.
Odermatt, D., Gitelson, A., Brando, V.E., Schaepman, M., 2012. Review of constituent retrieval in optically deep and complex waters from satellite imagery. Remote Sens. Environ. 118, 116–126.
Orlìc, M., Kuzmic, M., Pasaric, Z., 1994. Response of the Adriatic Sea to the bora and sirocco forcing. Cont. Shelf Res. 14 (1), 91–116.
Otero, P., Ruiz-Villarreal, M., Peliz, 2009. River plume fronts off NW Iberia from satellite observations and model data. ICES J. Mar. Sci.: J. du Conseil.
Pahlevan, N., Garrett, A.J., Gerace, A.D., Schott, J.R., 2012. Integrating Landsat-7 imagery with physics-based models for quantitative mapping of coastal waters near river discharges. Photogramm. Eng. Remote Sens. 78 (11), 1163–1174.
Pahlevan, N., Lee, Z., Wei, J., Schaaf, C.B., Schott, J.R., Berk, A., 2014. On-orbit radiometric characterization of OLI (Landsat-8) for applications in aquatic remote sensing. Remote Sens. Environ. 154, 272–284.
Pebesma, E.J., 2004. Multivariable geostatistics in S: the gstat package. Comput. Geosci. 30 (7), 683–691.
Petus, C., Marieu, V., Novoa, S., Chust, G., Bruneau, N., Froidefond, J.M., 2014. Monitoring spatio-temporal variability of the Adour river turbid plume (Bay of Biscay, France) with MODIS 250-m imagery. Cont. Shelf Res. 74, 35–49.
Petus, C., Chust, G., Gohin, F., Doxaran, D., Froidefond, J.-M., Sagarminaga, Y., 2010. Estimating turbidity and total suspended matter in the Adour river plume (South Bay of Biscay) using MODIS 250-m imagery. Cont. Shelf Res. 30 (5), 379–392.
Qin, B., Xu, P., Wu, Q., Luo, L., Zhang, Y., 2007. Environmental issues of lake taihu, China. Hydrobiologia 581 (1), 3–14.
R Cran Team, 2013. R: A Language and Environment for Statistical Computing.
Rao, Y.R., Schwab, D.J., 2007. Transport and mixing between the coastal and offshore waters in the Great Lakes: a review. J. Great Lakes Res. 33 (1), 202–218.
Robinson, I.S., 2010. Discovering the Ocean from Space: The Unique Applications of Satellite Oceanography. Springer Science & Business Media.
Ruddick, K., Lacroix, G., 2006. Current Status of Eutrophication in the Belgian Coastal Zone. Universitaires de Bruxelles Press, Belgium.
Shen, F., Zhou, Y., Li, J., He, Q., Verhoef, W., 2013. Remotely sensed variability of the suspended sediment concentration and its response to decreased river discharge in the Yangtze estuary and adjacent coast. Cont. Shelf Res. 69, 52–61.
Shen, P.-P., Li, G., Huang, L.-M., Zhang, J.-L., Tan, Y.-H., 2011. Spatio-temporal variability of phytoplankton assemblages in the Pearl River estuary, with special reference to the influence of turbidity and temperature. Cont. Shelf Res. 31 (16), 1672–1681.
Shen, F., Verhoef, W., Zhou, Y., Salama, M.S., Liu, X., 2010. Satellite estimates of wide-range suspended sediment concentrations in changjiang (Yangtze) estuary using MERIS data. Estuaries Coasts 33 (6), 1420–1429.
Sherwood, C.R., Carniel, S., Cavaleri, L., Chiggiato, J., Himangshu, D., Doyle, J., Harris, C., Niedoroda, A., Pullen, J., Reed, C., Russo, A., Sclavo, M., Signell, R., Traykovski, P., Warner, J., 2004. Sediment dynamics in the Adriatic Sea investigated with coupled models. Oceanography 17 (4), 46–57.
Solidoro, C., Bastianini, M., Bandelj, V., Codermatz, R., Cossarini, G., Canu, D.M., Ravagnan, E., Salon, S., Trevisani, S., 2009. Current state, scales of variability, and trends of biogeochemical properties in the northern Adriatic Sea. J. Geophys. Res.: Oceans 114 (C7).
Syvitski, J.P., Kettner, A.J., Correggiari, A., Nelson, B.W., 2005. Distributary channels and their impact on sediment dispersal. Mar. Geol. 222–223, 75–94.

Syvitski, J., Kettner, A.J., 2007. On the flux of water and sediment into the Northern Adriatic Sea. Cont. Shelf Res. 27 (3), 296–308.
Tesi, T., Miserocchi, S., Goni, M.A., Turchetto, M., Langone, L., De Lazzari, A., Correggiari, A., 2011. Influence of distributary channels on sediment and organic matter supply in event-dominated coastal margins: the Po prodelta as a study case. Biogeosciences 8 (2), 365–385. http://dx.doi.org/10.5194/bg-8-365-2011.
Trincardi, F., Cattaneo, A., Correggiari, A., 2004. Mediterranean prodelta systems: natural evolution and human impact investigated by EURODELTA. Oceanography 17 (4), 34–45. http://dx.doi.org/10.5670/oceanog.2004.02.
Van der Meer, F., 2012. 2012. Remote-sensing image analysis and geostatistics. Int. J. Remote Sens. 33, 5644–5676.
Vanhellemont, Q., Ruddick, K., 2016. ACOLITE for sentinel −2: aquatic applications of MSI imagery. ESA special publication. In: Presented at the ESA Living Planet Symposium Held in Prague. Czech Republic. pp. 9–13.
Vanhellemont, Q., Ruddick, K., 2015. Advantages of high quality SWIR bands for ocean colour processing: examples from Landsat-8. Remote Sens. Environ. 161, 89–106.
Vanhellemont, Q., Ruddick, K., 2014. Turbid wakes associated with offshore wind turbines observed with Landsat 8. Remote Sens. Environ. 145, 105–115.
Wang, S., Qian, X., Han, B.-P., Luo, L.-C., Hamilton, D.P., 2012. Effects of local climate and hydrological conditions on the thermal regime of a reservoir at Tropic of Cancer, in southern China. Water Res. 46 (8), 2591–2604.
Zhang, Y., Shi, K., Zhou, Y., Liu, X., Qin, B., 2016. Monitoring the river plume induced by heavy rainfall events in large, shallow, Lake Taihu using MODIS 250 m imagery. Remote Sens. Environ. 173, 109–121.
Zhang, Y., Shi, K., Liu, X., Zhou, Y., Qin, B., 2014. Lake topography and wind waves determining seasonal-spatial dynamics of total suspended matter in turbid Lake Taihu, China: assessment using long-term high-resolution MERIS data. PLoS One 9 (5), e98055.
Zhang, M., Tang, J., Dong, Q., Song, Q., Ding, J., 2010. Retrieval of total suspended matter concentration in the Yellow and East China Seas from MODIS imagery. Remote Sens. Environ. 114 (2), 392–403.
Zheng, Z., Li, Y., Guo, Y., Xu, Y., Liu, G., Du, C., 2015. Landsat-Based long-Term monitoring of total suspended matter concentration pattern change in the wet season for dongting lake, China. Remote Sens. 7 (10), 13975–13999.